

<https://doi.org/10.1038/s43247-024-01259-0>

Discovery of late Quaternary giant magnetofossils in the Bay of Bengal

Check for updates

Nitin Kadam^{1,2,3} ✉, Firoz Badesab¹ ✉, Ioan Lascu³, Courtney L. Wagner³, Virsen Gaikwad^{1,2}, Abhishek Saha¹, Satish Sangode⁴ & Mamilla Venkateshwarlu⁵

Unusually large and enigmatic giant magnetofossils are well-documented in sediments deposited during and surrounding climatic events such as the Paleocene-Eocene Thermal Maximum (~56 Ma) and Middle Eocene Climatic Optimum (~40 Ma). However, the absence of giant magnetofossil modern analogues raises intriguing questions about their origin and formation mechanism. In this study, we report the discovery of giant magnetofossils within late Quaternary sediments retrieved from the Bay of Bengal (BoB), the youngest giant magnetofossils yet reported. First-order reversal curve diagrams of BoB sediments display a central ridge feature, a characteristic magnetic signature of non-interacting single domain magnetofossils. Scanning electron microscopy examinations reveal giant magnetofossils with needle, spindle, bullet, and spearhead shapes. We use high-resolution transmission electron microscopy, with electron diffraction and energy dispersive spectrometry, to confirm their distinctive morphologies and magnetite crystal structure. Our environmental magnetic and geochemical data suggest that an influx of fluvially derived reactive iron and organic carbon, combined with persistent suboxic conditions, supported the proliferation of giant magnetofossil-producing organisms. The discovery of a modern analogue to ancient giant magnetofossils expands our understanding of their temporal distribution within the geological record and is a promising step toward elucidating the nature of the organisms responsible for their formation.

Magnetotactic bacteria are well known for their capacity to biomineralize nanometer-sized magnetic crystals, composed of magnetite or greigite, to navigate changing redox conditions in the water column or saturated sediment^{1–5}. These crystals are typically arranged in chain configurations within their cells which aids their navigation^{1–5}. After their death, the fossilized magnetic crystals, referred to as magnetofossils, contribute to the sedimentary magnetic signal^{6–8}. The preservation and characteristics of magnetofossils over geological time can serve as valuable indicators of paleoenvironmental change (including changes in redox conditions)^{9–12}, microbial ecosystem dynamics¹³, and the geomagnetic field variability^{14,15}.

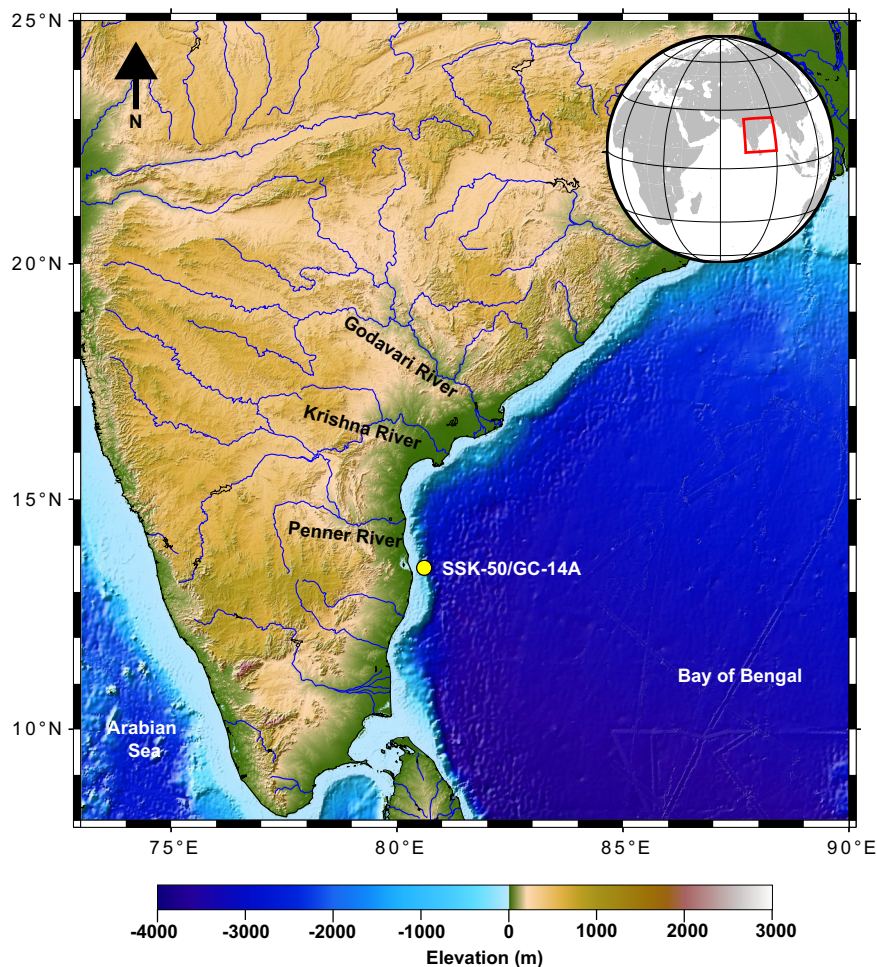
Previous research has linked bacterial iron biomineralization to various processes and events, including hyperthermal events^{10,11,16,17}, cometary impacts (occurrence of single domain magnetic particles)^{18,19}, alterations in weathering and sedimentation patterns^{20–23}, paleoproductivity^{24–30}, the development of thick suboxic zones³¹, and changes in oceanic ventilation³².

Of particular interest are exceptionally large biogenic magnetic crystals, known as giant magnetofossils, whose origin has long remained a mystery. Giant magnetofossils have been identified in sediments from the Late Paleocene, during the Paleocene-Eocene Thermal Maximum and during the Middle Eocene Climatic Optimum events, with no known modern analogues^{10,16,33–37}. This enigma has led to the assumption that extreme warming periods create the necessary conditions for the proliferation of giant magnetofossil-producing organisms.

In this study, we present the discovery of giant magnetofossils in late Quaternary sediments from the Bay of Bengal (BoB) (Fig. 1). We substantiate this discovery with magnetic analyses (including first-order reversal curve (FORC) datasets) and a suite of electron microscopy (with elemental and crystallographic information). Furthermore, we elucidate the environmental conditions that may have been both favourable and conducive to the growth and preservation of giant magnetofossil producing organisms.

¹CSIR-National Institute of Oceanography, Dona Paula, Goa, India. ²School of Earth Ocean and Atmospheric Sciences, Goa University, Goa, India. ³Department of Mineral Sciences, National Museum of Natural History, Smithsonian Institution, Washington, DC 20560, USA. ⁴Department of Geology, Savitribai Phule Pune University, Pune, India. ⁵CSIR-National Geophysical Research Institute, Hyderabad, India. ✉e-mail: nbkadam@nio.org; firoz@nio.org

Fig. 1 | Location of the studied sediment core (SSK-50/GC-14A) from the BoB. Elevation map of the BoB displaying the location of the sediment core (denoted by a yellow filled circle). Sediments deposited at the core site originate predominantly from the Godavari, Krishna, and Penner Rivers, highlighted on the map. The map is created using SRTM15 + V2.4 datasets⁶⁶ with pygmt v0.9.0.



Results

Physical, bulk magnetic and geochemical properties of BoB sediments

The sediment core consists mainly of pale green silty clays. The proportion of sand in the core remains minimal except for a relative increase during the Late Glacial period. Additionally, a darkening of sediment colour is noted in the lower section of the sediment core. Microscopic observations of the coarse sediment fractions reveal an abundance of both benthic and planktic foraminifera.

Magnetic parameters within the sediment core display notable downcore variability (Fig. 2). Magnetic mineral concentration-dependent parameters (magnetic susceptibility (χ_{lf}) and saturation magnetization (M_s)) show an increase during the Last Glacial Maximum (~25–15 ka) and the Holocene (~10–2 ka) (Fig. 2a, e). This observation generally aligns with the downcore variations in iron (Fe%) content (Fig. 2j). The anhysteretic susceptibility (χ_{ARM}) to saturation isothermal remanent magnetization (SIRM) ratio, a magnetic grain size indicator, exhibits values ranging from 1.2–3.6 mm/A (~42.7–2 ka), indicative of non-interacting single domain magnetite³⁸ (Fig. 2b). End member unmixing of SIRM curves elucidates the downcore variability of magnetic minerals using a combination of four end members (Supplementary Figs S1 and S2). A minimum in magnetic mineral concentration is noted during the Late Glacial ($\chi_{lf}(\text{minimum}) = 9.46 \times 10^{-8} \text{ m}^3/\text{kg}$) (Fig. 2a). There is an increase in χ_{ARM}/SIRM , coercivity of remanence (B_{cr}), and the remanence ratio (M_r/M_s) over the same interval (Fig. 2b, d, f). Although SIRM values are low over this interval, there is an overall increase in the relative contribution of magnetic end member M-III to SIRM (Fig. 2g). M-III, interpreted to be a magnetofossil-rich end member, contributes 86.53% to the total SIRM during the Late Glacial (Fig. 2g and Supplementary Fig. S2). The Late Glacial appears to be a period of

reduced detrital magnetic mineral input coincident with an increase in the relative abundance of magnetofossils. Magnetofossil abundance is also high during most of the LGM (Fig. 2g and Supplementary Fig. S2). The notable predominance of magnetic end member M-III during the LGM and Late Glacial hints to the dominant presence of magnetofossils during this time (Supplementary Fig. S2). Magnetofossils that maintain a single domain state based on their size and domain energy budget contribute to M-III, while those that do not meet this criterion would contribute to the other end members. M-I, M-II, and M-IV represent detrital magnetic components primarily derived from catchment rock erosion (Supplementary Fig. S2). The oldest sediments (>30.1 ka) exhibit low magnetic mineral concentration (Fig. 2a, e). This section of the sediment core has low χ_{ARM}/SIRM and S-ratio values (Fig. 2b, c). Accordingly, the relative contribution of high coercivity magnetic end member M-IV increases during this period (Supplementary Fig. S2).

The magnetization values exhibit a notable decrease around 560 °C in all sediment samples, indicating the presence of magnetite (Curie temperature of magnetite ~575 °C) (Supplementary Fig. S3). Sediments younger than 30.1 ka display small differences between pre- and post-heating magnetization values (Supplementary Fig. S3a–c). Conversely, in the case of the oldest sediments (>30.1 ka), considerable magneto-mineralogical alterations occur during heating, and the irreversible cooling curve concludes with substantially higher magnetization values (Supplementary Fig. S3d). This implies that the magnetic mineral assemblage of the oldest sediments is different than the other intervals possibly due to post-depositional alterations (Supplementary Fig. S3).

The organic carbon content in the sediment core is low (<3%) and has a decreasing trend until the Holocene, where it slightly increases (Fig. 2h). Calcium carbonate content fluctuates between 0 and 50% and exhibits a

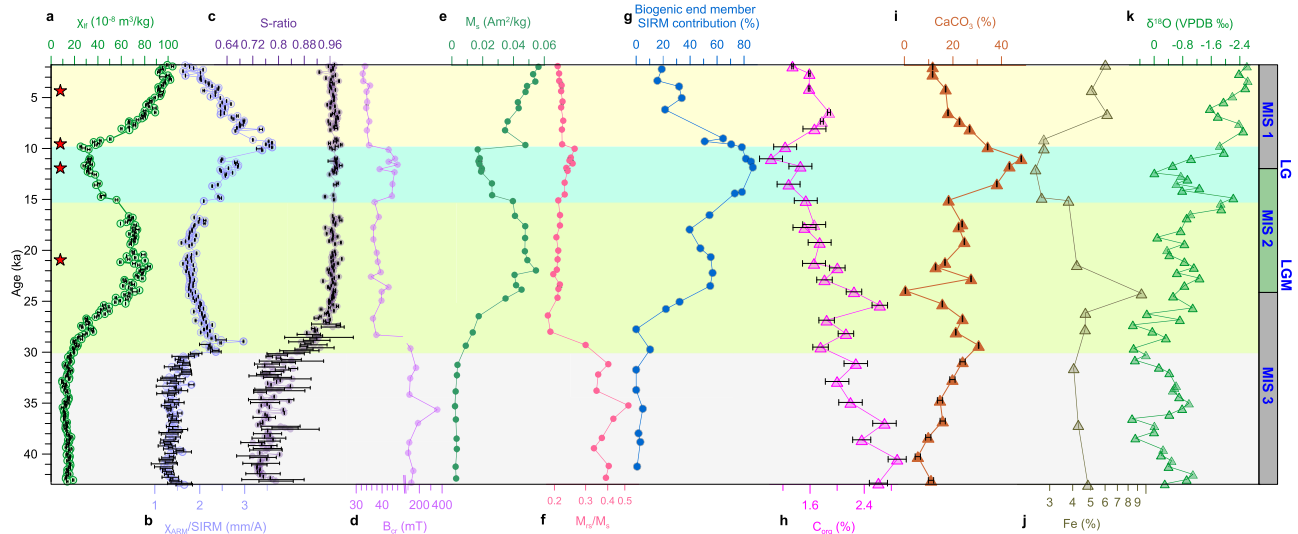


Fig. 2 | Downcore magnetic and geochemical profile for the late BoB sediments.

a magnetic susceptibility ($\chi_{f, 10^{-8} \text{ m}^3/\text{kg}}$), **b** magnetic grain size parameter ($\chi_{\text{ARM}}/\text{SIRM}$; mm/A), **c** magnetic mineralogy indicative parameter (S-ratio), **d** coercivity of remanence (B_{cr} ; mT), **e** saturation magnetization (M_s ; Am^2/kg), **f** magnetic remanence ratio (M_{rs}/M_s), **g** Biogenic end member SIRM (M-III) contribution (%), **h** total organic carbon content (C_{org} ; %), **i** calcium carbonate content (CaCO_3 ; %), **j** iron concentration (Fe; %), **k** published bulk sediment oxygen isotope data ($\delta^{18}\text{O}$; ‰

VPDB)⁵⁹ (Reprinted with permission from Current Science). Error bars are included to represent the relative errors for magnetic parameters, while the standard deviation ($\pm \text{S.D.}$) is utilized to depict the uncertainty in geochemical parameters. The Marine Isotopic Stages (MIS) and the Late Glacial (LG) and Last Glacial Maximum (LGM) time periods are shown. Red coloured stars indicate the sediment intervals selected for TEM analysis. Coloured bands show significant variations in the magnetic and geochemical parameters.

general increasing trend in the Late Pleistocene, followed by a decrease during the Holocene (Fig. 2i). The $\delta^{18}\text{O}$ downcore profile of the sediment core closely mirrors temperature fluctuations during major climatic events, including the LGM and the Late Glacial (Fig. 2k).

FORC diagrams

The FORC diagrams display a prominent central ridge along the horizontal axis, a characteristic that serves as a diagnostic indicator of non-interacting single domain particles (Fig. 3a–f). The wide range in coercivity observed in the coercivity distributions along the central ridges may be caused by mixtures of biogenic soft (BS), biogenic hard (BH), and biogenic needle (BN) magnetofossil components (Supplementary Fig. S4). Conventional magnetofossils can be categorized into two groups based on coercivity: biogenic soft (BS; 10–50 mT) and biogenic hard (BH; 50–100 mT) magnetofossils, corresponding to different magnetofossil morphologies³⁹. Horizontal coercivity profiles along the central ridge show presence of BS and BH components (Supplementary Fig. S4). The distinction between BS and BH is due to crystal anisotropy, linked to differences in crystal shape: the BS component is characterized by equant magnetofossils, while the BH component is dominated by elongated magnetofossils³⁹. However, the collapse and disruption of linear magnetosome chain arrangement reduces the median coercivity values⁴⁰. Differences in number, spacing, and arrangement of magnetofossils, which could contribute to the BS and BH components⁴¹. Notably, our electron microscopy results confirm the presence of both equant and elongated magnetofossils, which could contribute to the BS and BH components (Supplementary Fig. S5). Ref. 34 previously identified a biogenic needle (BN) component, with a higher median coercivity than BS and BH, ascribed to the presence of giant needles. Some of our samples (Supplementary Fig. S4c–e) also contain a higher coercivity component (~120 mT), which we attribute to the BN component. There is also a low coercivity component, with the peak around 10–15 mT, indicating a detrital magnetic component (Supplementary Fig. S4). The detrital material is identified in the FORC diagram by the spread along the vertical axis in the upper halfplane, and the lobe-like contour pattern in the lower halfplane of the FORC diagram, suggesting a substantial non-single domain contribution (Fig. 3a–e), consistent with our IRM unmixing results (Supplementary Fig. S2). The FORC diagram of the sediment sample from the lower section

of the sediment core (>30.1 ka) shows a central ridge dominated by a component with very low coercivity (Fig. 3f and Supplementary Fig. 4f). The presence of a vertical ridge along the B_u axis in the lower half plane suggests this component could be ultrafine, superparamagnetic-single domain grains with an authigenic origin. Additionally, contours extending beyond 160 mT below the B_c axis suggest the presence of a higher coercivity component of detrital nature, likely haematite (Fig. 3f).

Electron microscopy

Transmission electron microscopy (TEM) of magnetic extracts from the LGM, Late Glacial, and Holocene sediment intervals reveal an abundance of conventional magnetofossils with prismatic, bullet, teardrop, and cuboctahedral shapes (Supplementary Fig. S5). Scanning electron microscopy (SEM) images confirm the presence of conventional magnetofossils (Supplementary Fig. S6c, S6e, and S6f). Similarly, we identify giant magnetofossils, including needles and giant bullets, and determine their chemical composition using TEM-energy dispersive spectra (Figs. 4 and 5). Giant needles are found in the magnetic extracts from the LGM, Late Glacial, and Holocene sediment intervals and have dimensions ranging from ~1000–1250 nm in length and ~80–120 nm in width (Fig. 4a, h, j, k). Similarly, giant bullets are identified in Late Glacial and Holocene sediment intervals and display dimensions ranging from a ~913–1400 nm in length and ~283–320 nm in width (Fig. 4c, e). Giant magnetofossils with spindle, needle, bullet, and spearhead shapes are also observed in the magnetic extracts from the LGM and Late Glacial sediment intervals during SEM imaging (Fig. 6). We identify a spearhead-shaped magnetic particle, ~4760 nm in length and ~1060 nm in width, featuring crystal faces on the apex portion and circumferential steps on the middle and lower (stalk) sectors (Fig. 6a), akin to observations by ref. 33. Notably, this spearhead has an additional, unusual stalk-like feature, ~1300 nm in length (Fig. 6a). Spindle-shaped crystals, with lengths of ~3000 nm and widths of ~500 nm is tapered at both ends and display crystal faces (Fig. 6b, f).

The lattice fringes of conventional magnetofossils have d-spacing values of 4.8 Å and 2.5 Å, corresponding to the 111 and 311 planes of magnetite, confirming their crystallographic structure (Supplementary Fig. S5i, S5k). Energy dispersive spectroscopy (EDS) analysis on giant magnetofossils show strong iron and oxygen peaks indicating their iron

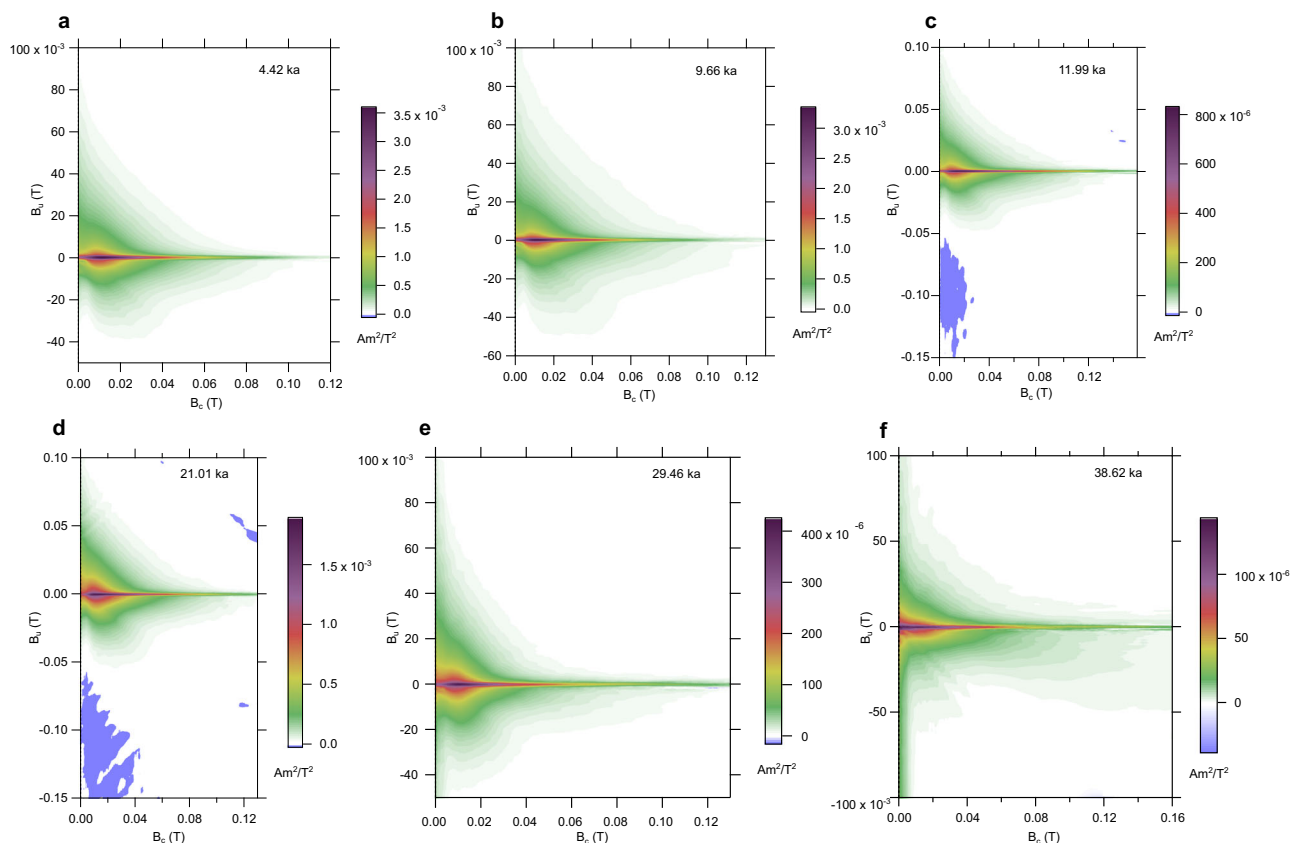


Fig. 3 | First-order reversal curve (FORC) diagrams of representative sediment samples from the late Quaternary BoB sediments. a–e FORC diagrams displaying a central ridge feature along the horizontal axis ($B_h = 0$). The central ridge feature is a characteristic of non-interacting single domain magnetofossils. **f** The presence of a

vertical ridge along the B_v axis in the lower half plane suggests a ultrafine, superparamagnetic-single domain component with an authigenic origin. Additionally, contours extending beyond 160 mT below the B_h axis suggest the presence of a higher coercivity component of detrital nature, likely haematite.

oxide composition (Figs. 5–7), and lattice fringes show d-spacing of 4.8 Å, 1.6 Å and 2.9 Å for the giant needles and bullets, corresponding to 111, 511 and 220 planes of magnetite, respectively (Fig. 4b, d, f, i). Additionally, selected area electron diffraction (SAED) patterns collected on giant magnetofossils indicates a d-spacing of 2.9 Å corresponding to the 220 plane of magnetite (Fig. 4g, l). The energy dispersive spectrum obtained on the apex portion of the spearhead-shaped giant magnetofossil indicates iron oxide composition (Fig. 7a). The crystal morphology, purity of chemical composition, and lattice perfection of magnetite in the giant needles are confirmed through HRTEM analysis, establishing their biological origin. The sizes, shapes, and compositions are consistent with previously identified conventional and giant magnetofossils^{10,16,33–37}.

Discussion

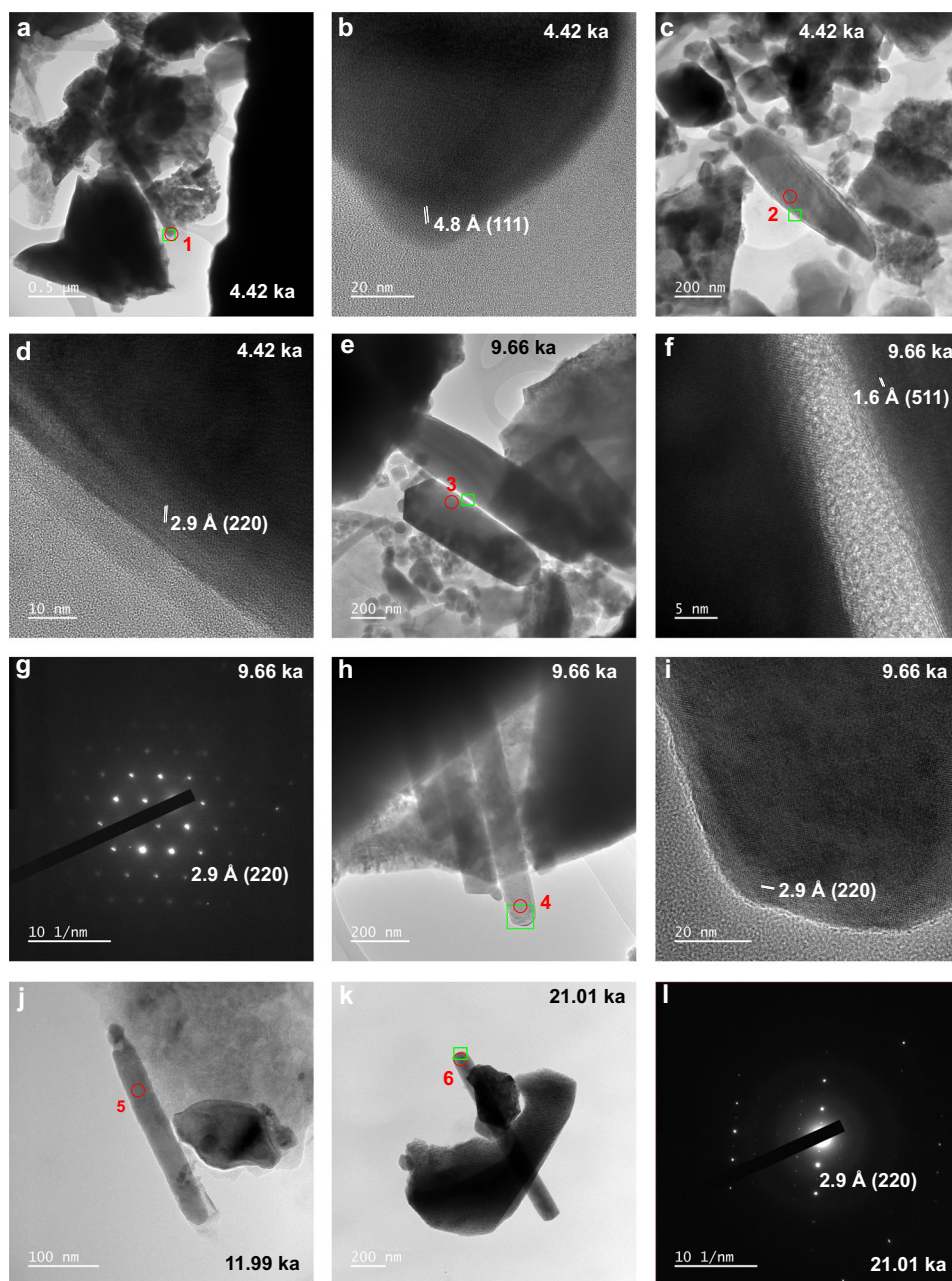
Initially documented and described by ref.³³, giant magnetofossils have been identified in sediments dating from ~56–46 million years ago^{10,16,33–37}. More recently, ref.³⁷ reported the presence of giant magnetofossils in North Atlantic pelagic sediments, both within and outside of the Paleocene-Eocene Thermal Maximum, underscoring that their origin is not exclusively linked to ancient hyperthermal events. However, there have been no prior reports of giant magnetofossils in geologically recent sediments. In this study, we present several lines of evidence for giant magnetofossils in late Quaternary sediments retrieved from the BoB. Our findings are supported by a combination of magnetic parameters (Fig. 2), electron microscopy (Figs 4–7 and Supplementary Figs S5–S6), and FORC diagrams (Fig. 3), all of which collectively confirm the existence of both conventional and giant magnetofossils. The morphologies of the giant magnetofossils observed in our electron micrographs are consistent with those documented previously^{10,16,33–37}. Further validation is provided by HRTEM (lattice fringe

analysis), SAED, and EDS data which all confirm magnetite composition (Figs 4–7 and Supplementary Figs S5–S6). The length and axial ratio (width/length) of giant needles imply their existence in a stable single-domain state, while giant bullets exist in a vortex state⁴². The large sizes of spearhead-shaped giant magnetofossils do not allow them to be in single domain configurations. Instead, they likely adopt vortex or multidomain states. The dimensions of identified spindle-shaped crystals lie within the vortex state of magnetite⁴².

The electron microscopy analysis of the magnetic particles indicates that diagenesis (i.e., reductive dissolution) did not significantly affect the sediment magnetic record in the last ~30 ka. In our SEM analysis, we observed cracks (Supplementary Fig. S7), and a pitted appearance on the surfaces of a small number of detrital magnetic particles, possibly suggesting the influence of only mild physical and chemical weathering affecting these particles during their transit from source to sink. The presence of pyrite in the lower section of the sediment core indicates reducing conditions prior to 30.1 ka, likely a result of diagenesis (Supplementary Fig. S7). Magnetofossil preservation under such conditions would have been minimal.

The Bay of Bengal is distinguished by the presence of a distinctive oxygen minimum zone (OMZ) at mid-depth in its waters. Prior research on BoB sediments has indicated a strengthening of the northeast and southwest monsoons during the LGM and Holocene, respectively, which significantly drove weathering and sedimentation along the continental margins of India^{43–46}. The strengthening of the monsoon enhances weathering and erosion in the source regions, leading to the discharge of terrigenous material and organic matter into the BoB. Significant sea level drop occurred during the LGM, resulting in the exposure of shelf regions to erosion and contributing to sedimentation along the western continental margin of India^{47,48}. Here, we observe large proportions of detrital magnetic minerals

Fig. 4 | HRTEM images, lattice fringes and SAED patterns of giant magnetofossils from the late Quaternary BoB sediments. **a** A giant needle measuring ~1250 nm in length and ~120 nm in width. **b** Lattice fringe value (4.8 Å) and the corresponding Miller index (111) for the giant needle shown in (a). **c** A giant bullet with dimensions of ~790 nm in length and ~210 nm in width with several conventional magnetofossils. **d** Lattice fringe value (2.9 Å) and the corresponding Miller index (220) for the giant bullet shown in (c). **e** Two giant bullets with one measuring ~913 nm in length and ~283 nm in width, and another measuring ~1400 nm in length and ~320 nm in width along with several conventional magnetofossils. **f** Lattice fringe value (1.6 Å) and the corresponding Miller index (511) for the giant bullet shown in (e). **g** Selected area electron diffraction pattern showing d-spacing value (2.9 Å) for the giant bullet shown in (e). **h** A bunch of giant needles exceeding ~1000 nm in length and ~120 nm in width adhered to other mineral phases. **i** Lattice fringe value (2.9 Å) and the corresponding Miller index (111) for the giant needle shown in (h). **j** A short needle measuring ~310 nm in length and ~40 nm in width. **k** A giant needle measuring ~1100 nm in length and ~100 nm in width adhered to other mineral phases. **l** SAED pattern showing d-spacing value (2.9 Å) for the giant needle shown in (k). The lattice fringes and SAED pattern corresponds to magnetite. Light green-coloured rectangles indicate the regions where the lattice fringes and SAED are obtained. Red circles indicate the regions where EDS is obtained. The numbers highlighted in red represent EDS, as depicted in Fig. 5.



over the LGM and Holocene intervals within this core which are consistent with monsoonal trends, and a decrease in detrital magnetic particles between ~15–10 ka is consistent with a decrease in weathering and erosion over the Late Glacial Period (Fig. 2). Interestingly, we found no correlation between the biogenic magnetic end member (M-III) and variations in organic carbon content within the sediment core (Fig. 2g–h). Although marine productivity was notably high during the late glacial period, it decreased during the LGM (Fig. 2i). The presence of conventional magnetofossils implies that suboxic conditions prevailed since 30.1 ka. Despite variations in the organic carbon and iron content within the sediment core, it seems that their concentrations were adequate for the organisms responsible for producing the giant and conventional magnetofossils. There is no existing research documenting the occurrence of giant magnetofossils without the simultaneous occurrence of conventional magnetofossils. This suggests that conditions favourable for the development of magnetotactic bacteria are essential for the organisms responsible for producing giant magnetofossils. We propose that an ample supply of reactive iron from

nearby riverine systems in the BoB, which became bioavailable due to mild suboxic diagenetic conditions, combined with the availability of organic carbon as a food source, favoured the growth of the giant magnetofossil-producing organisms. In the present scenario, the conditions for iron and organic carbon availability from fluvial sources, concerning the formation of giant magnetofossils, align with previous research^{20,33}. However, it is crucial to note that their presence is not exclusively associated with the climatic warming events, as we have found giant magnetofossils in sediments deposited at the height of the last glaciation. We suggest that as long as the aforementioned conditions persist, the organisms responsible for producing giant magnetofossils will thrive.

We now elucidate the mechanisms sustaining persistent suboxic conditions in the BoB, which likely facilitated the development of organisms contributing to the formation of giant magnetofossils. Furthermore, we propose that these conditions have endured since the late Quaternary, despite fluctuations in several crucial interconnected factors. The studied sediment core is situated within the present-day OMZ of the BoB. OMZs are

Fig. 5 | Energy dispersive X-ray spectra for the giant magnetofossils from the late Quaternary BoB sediments. a–f depict the EDS spectra corresponding to the giant magnetofossils highlighted in red-numbered order in Fig. 4. The spectra's display prominent iron and oxygen peaks, confirming the iron oxide composition of the giant magnetofossils. The copper peak originates from the TEM grids, while the carbon peak arises from the carbon film on the TEM grid.

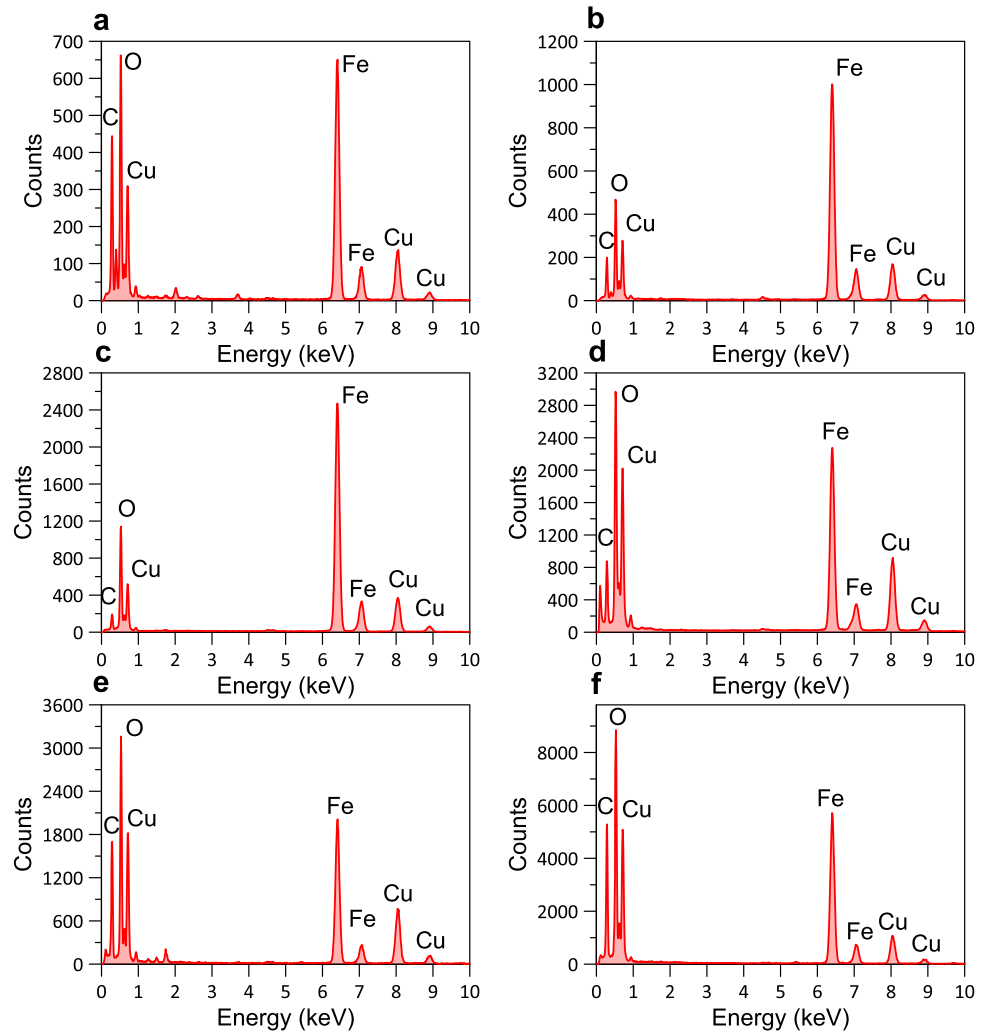


Fig. 6 | SEM images of different types of giant magnetofossils from the late Quaternary BoB sediments. a Spearhead-shaped giant magnetofossil with circumferential feature and a long stalk. The spearhead-shaped giant magnetofossils is ~4760 nm in length and ~1060 nm in width. **b** A spindle-shaped giant magnetofossil on the surface of a large detrital magnetic mineral. The length and width of spindle-shaped giant magnetofossils is ~3000 nm and ~500 nm, respectively. **c** A giant bullet resting on the TEM copper grid measuring ~1500 nm in length and ~230 nm in width. **d, e** Giant needles on the surface of other magnetic mineral phases. The length and width of the giant needles ranges from ~1000–1374 nm and ~120–150 nm. **f** A spindle shaped giant magnetofossil measuring ~2900 nm in length and ~480 nm in width. Red circle indicates the position where the energy dispersive X-ray spectra is obtained.

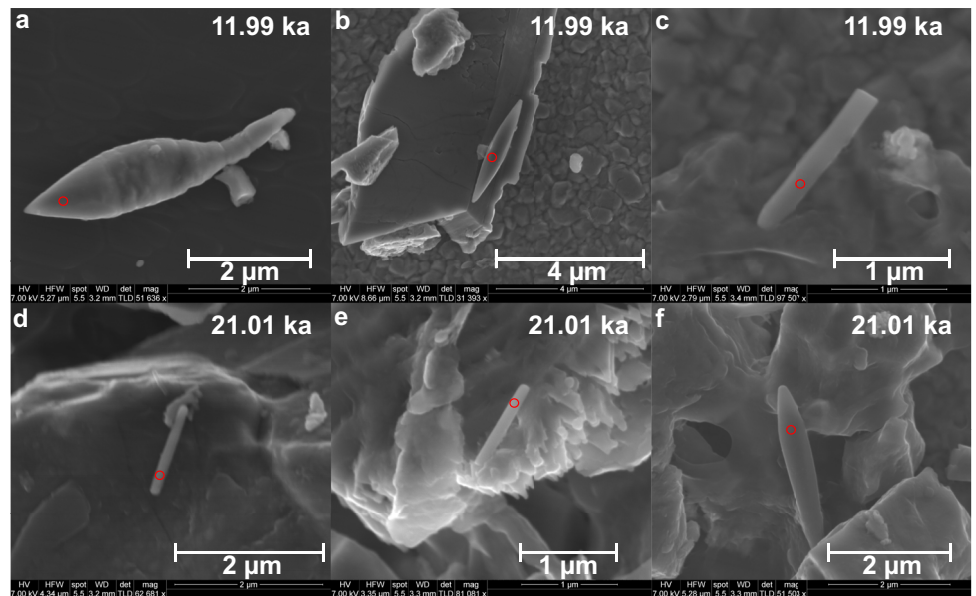
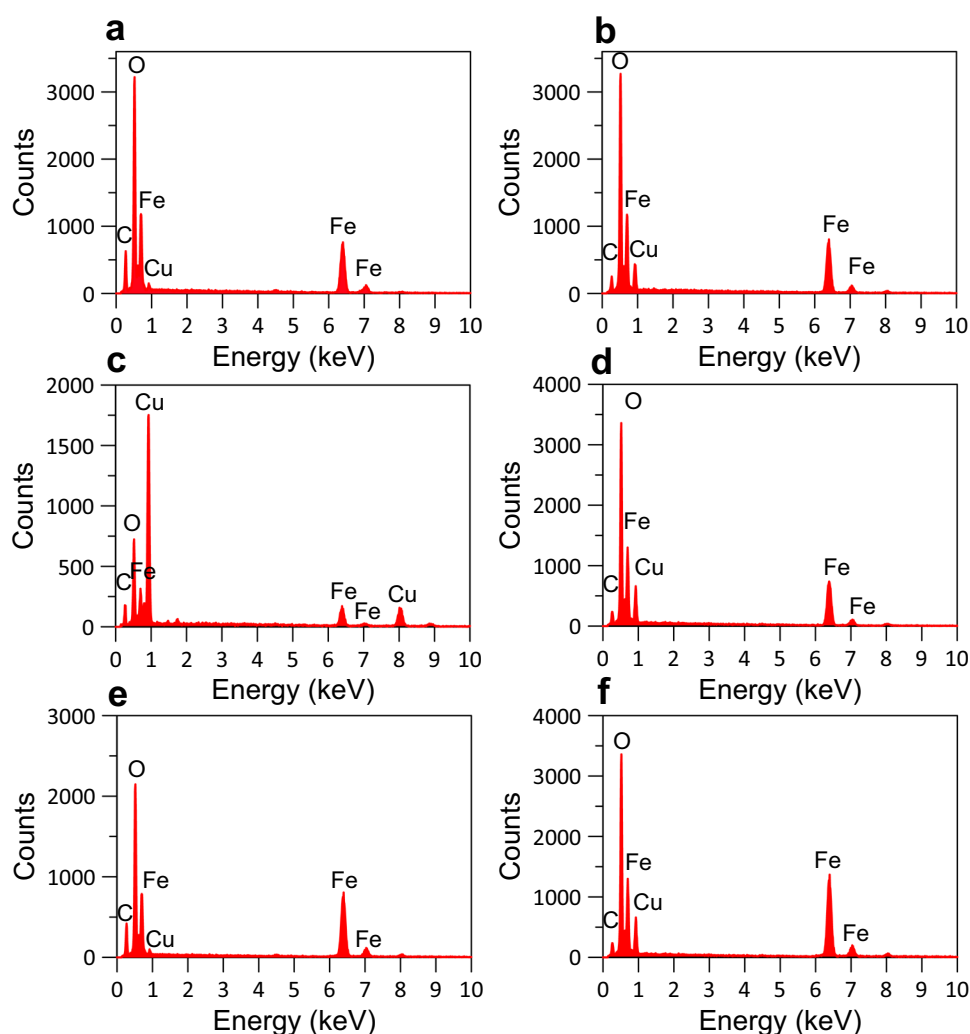


Fig. 7 | Energy dispersive X-ray spectra for different types of giant magnetofossils from the late Quaternary BoB sediments. a–f depict the EDS spectra corresponding to the giant magnetofossils highlighted in Fig. 6a–f. The spectra's show prominent iron and oxygen peaks, confirming the iron oxide composition of the giant magnetofossils. The copper peak originates from the TEM grids.



characterized by consistently low oxygen concentrations in seawater at intermediate depths of the water column (~1000–1300 m)⁴⁹. These zones are prevalent in various regions, including the Eastern North Pacific, Eastern South Pacific, Arabian Sea, and BoB. In the northern Indian Ocean, the Arabian Sea exhibits dissolved oxygen concentrations below 2 μM (0.05 ml/L), while in the BoB, it is below 4 μM (0.1 ml/L) at intermediate water column depths (~100–1000 m)⁵⁰. The BoB stands out for its unique oxygen content in its waters, primarily due to the substantial sediment load brought in by major rivers like the Ganges-Brahmaputra, Krishna-Godavari, Mahanadi, Penner, and Cauvery. These rivers play a crucial role in delivering essential nutrients, including iron and oxygen, to the BoB. While the overall primary productivity in the BoB is low, the strong salinity stratification resulting from the massive freshwater discharge from these rivers, combined with physical oceanographic processes like eddy formation, contributes to oxygen introduction into the water column^{51–54}. This dynamic maintains suboxic conditions in the BoB, distinct from the intense oxygen minimum zones (strong anoxia) observed in the rest of oceans dominated by OMZs, which are unfavourable for the growth of magnetotactic bacteria and their subsequent preservation. The continuous maintenance of these parameters in the BoB likely facilitated the proliferation of giant magnetofossil-producing organisms, in conjunction with magnetotactic bacteria. Research employing foraminiferal abundance, redox-sensitive geochemical analyses, and oxygen isotopic compositions in sediment cores from the western BoB adjacent to our studied core indicates significant alterations in monsoonal intensity, terrigenous input, nutrient supply, hydrographic structure, sea level, and redox conditions since the late

Quaternary time^{47,55,56}. These studies provided a mixed interpretation on the oxic-suboxic-anoxic conditions in the BoB during the late Quaternary period^{47,55,56}. However, the presence of magnetofossils, both conventional and giant, in the studied core over the past ~30 ka confirms the persistence of suboxic conditions in the southwestern BoB. We suggest that the interplay of these intricate parameters contributed to the sustained suboxic conditions with an abundant supply of essential nutrients such as reactive iron and organic carbon from the riverine input. These environmental conditions likely fostered the growth of organisms responsible for producing giant magnetofossils. Moreover, our results align with a recent investigation, which utilized environmental magnetic parameters, geochemical parameters, and clay mineralogy to reveal the continuous presence of suboxic conditions in the BoB over the last 52 ka⁵⁷. These findings in combination with our results suggest that similar conditions are likely maintained in the present day, offering an opportunity to explore the organisms responsible for the formation of these giant crystals. This discovery further poses several research questions including the co-existence of the conventional and giant magnetofossils species; the equilibrating conditions of reactive iron-organic carbon and oxygen minima to be explained for the growth of magnetotactic bacteria and giant magnetofossils producing organisms.

Methods

Sediment core collection and subsampling

A gravity sediment core (SSK-50/GC-14A), 2.82 m in length, was retrieved from the southwestern BoB (13°29'12"N, 80°34'30"E, water depth = 325

metres; Fig. 1) onboard Indian research vessel R/V Sindhu Sankalp. After the completion of coring operation, the sediment core was cut into 1 metre sections and immediately stored at -20°C in a refrigerator onboard. Subsequently, the core sections were transferred to the cold repository of the CSIR-National Institute of Oceanography (CSIR-NIO) in Goa, India. Subsampling was conducted at 1–2 cm interval along the core. Each subsample was placed in glass containers and dried at 40°C for 10–12 h. The dried subsamples were then packed into non-magnetic cylindrical bottles for magnetic measurements. Prior to packing, the weights of the sediment samples were recorded for subsequent mass-normalization purposes. Representative samples were homogenized and carefully packed into gelatin capsules for hysteresis, direct current demagnetization (DCD) and FORC measurements.

Age model

The chronology of the sediment core (SSK-50/GC-14A) was established by ref. 58 using the $\delta^{18}\text{O}$ correlation between adjacent sediment cores. The age model relies on the radiocarbon dating of mixed planktonic foraminifera from the upper and lower sections of the sediment core, which were analyzed at the NSF Arizona AMS Laboratory⁵⁹. The measured radiocarbon ages were corrected for a reservoir age of 331 years estimated for the western BoB, north of Sri Lanka, as reported by ref. 60. These ages were then converted into calendar ages using the CalPal-7 calibration. The robustness of the chronology was assessed by ref. 58 by comparing the mixed layer $\delta^{18}\text{O}$ record of SSK-50/GC14A with other $\delta^{18}\text{O}$ records from the BoB region and the GISP2 $\delta^{18}\text{O}$ record, demonstrating strong correlation during major climatic periods. Additional information regarding the chronology of the sediment core can be found in the references ref. 58 and ref. 59.

Rock magnetic experiments

Magnetic susceptibility measurements were performed on a Bartington Instrument MS2B dual frequency susceptibility meter operating at low frequency [χ_{lf} (0.47 kHz)]. Standard magnetite sample was used to calibrate the instrument (3072×10^{-5} SI at 22°C , accuracy: 0.046%). Each sediment sample was measured thrice, and the average values were used for further calculations. A Molspin alternating field (AF) demagnetizer was used to induce the anhysteretic remanent magnetization (ARM) by applying an alternating magnetic decaying from a field of 100 mT, superimposed on a $50 \mu\text{T}$ bias direct current magnetic field. Isothermal remanent magnetization (IRM) was imparted using a MMPM10 pulse magnetizer by applying direct current pulse fields in the forward direction and was subsequently demagnetized in backfields of -20 mT, -30 mT, -100 mT, and -300 mT. A JR-6A automatic dual speed spinner magnetometer (AGICO, Czech Republic) was used to measure the ARM and IRM in two position settings and the relative error was estimated. Prior to these measurements, the instrument was calibrated using a magnetite standard (Magnetization: 6.11 A/m, accuracy: 0.16%), followed by the application of a holder correction to eliminate the influence of plastic magnetic bottles. The magnetization measured at a peak field of 2.5 T was considered to be the saturation isothermal remanent magnetization (SIRM). Magnetic susceptibility and remanence values were mass normalized. The magnetic mineralogy sensitivity parameter S-ratio was calculated following the equation $S\text{-ratio} = [1 + (-\text{IRM}-300\text{mT}/\text{SIRM})] / 2$. Anhysteretic susceptibility (χ_{ARM}) was calculated by normalizing ARM values by the $50 \mu\text{T}$ bias field. The IRM acquisition curves were performed on a set of 30 representative samples. A series of thirty DC pulse magnetic fields with increasing magnitude were sequentially applied (maximum field = 2.5 T). The MMPM10 pulse magnetizer was used to induce the magnetic fields. All magnetic susceptibility and remanence experiments were performed at the paleomagnetic laboratory of CSIR-National Institute of Oceanography (CSIR-NIO), Goa, India. Thermomagnetic curves (temperature range: $0\text{--}700^{\circ}\text{C}$) were performed on representative sediment samples using advance variable field translation balance (AVFTB) at CSIR-National Institute of Geophysical Research (CSIR-NGRI), Hyderabad, India.

Hysteresis loops, DCD curves, and first-order reversal curves were measured on the Lake Shore 8604 vibrating sample magnetometer at the National Museum of Natural History, Smithsonian Institution, Washington DC. Hysteresis loops were measured for 41 sediment samples using a saturating field of 1 T, a field increment of 5 mT, and an averaging time of 0.25 s. The hysteresis loops were corrected to account for any paramagnetic contributions evident at high magnetic fields. Subsequently, saturation remanence and coercivity were estimated from the corrected hysteresis loops. The coercivity of remanence was calculated from DCD curves (saturation field = 1 T, averaging time = 3 s, logarithmic field increment, number of steps = 100).

FORCs were measured on six samples. A total of three hundred and thirty-one FORCs were acquired for each sample using the following experimental parameters: B_c range of (0, 160 mT), B_u range of (-50 , 120 mT), a saturation field of 1 T, a field increment of 1 mT, and an averaging time of 0.25 s. The resulting FORC diagrams were processed utilizing the VARIFORC protocol⁶¹ in FORCinel software version 3.06⁶². During data processing, specific smoothing factors were applied, including a vertical ridge (S_{c0}) of 7, horizontal smooth (S_{c1}) of 7, central ridge (S_{b0}) of 3, vertical smooth (S_{b1}) of 7, horizontal lambda of 0.1, vertical lambda of 0.1, and central ridge vertical offset of 0.

It is important to note that a different set of parameters was employed for sediment sample from the lower section of the sediment core (at 38.62 ka). For this particular sample, an identical number of three hundred and thirty-one FORCs were measured, albeit with adjusted parameters. These adjustments included B_c range of (0, 175 mT), B_u range of (-50 , 120 mT), a saturation field of 1 T, a field increment of 1 mT, and a longer averaging time of 0.5 s. The processing of FORCs for this sample involved alternative smoothing factors, including a vertical ridge (S_{c0}) of 9, horizontal smooth (S_{c1}) of 9, central ridge (S_{b0}) of 3, vertical smooth (S_{b1}) of 9, horizontal lambda of 0.125, vertical lambda of 0.125, and central ridge vertical offset of 0.

Magnetic end member analysis

Originally based on the algorithm developed by ref. 63, end member analysis uses a non-negative matrix factorization algorithm to unmix the magnetic remanence data⁶⁴. It is an inverse technique to decompose magnetic data into meaningful components. The non-negative matrix factorization algorithm does not require any basis functions to fit the data and uses the variability observed in data to unmix the curves. The algorithm can be expressed in the matrix form as

$$X = AS + \varepsilon$$

X is an observation matrix ($n \times m$) in which n rows contain observations (samples), and m columns contain variables (IRM fields). A is an end member abundance matrix ($n \times k$) in which k represents the number of end members in the column. S is an end member property matrix ($k \times m$). The error matrix (e.g., instrumental noise) is represented by ε . The algorithm proposed the inclusion of a non-negativity constraint, as suggested by ref. 64, to ensure that the contributions of the end members are strictly positive values. IRM Unmixer code performs principal component analysis and calculates the coefficient of determination (R^2) with the increasing number of components. In order to ensure geological interpretability and environmental soundness, the selection of end members must prioritize maximizing the R^2 values.

Geochemistry

About fifteen representative sediment samples were manually powdered in an agate mortar. After every sample, the agate mortar and pestle were first washed with distilled water, then cleaned with acetone and later with diluted hydrochloric acid to avoid cross contamination. The homogeneity of the prepared samples was ensured. The powdered samples were analysed for

major oxides along with matrix matching geochemical reference materials for quality control at CSIR-National Geophysical Research Institute (CSIR-NGRI), Hyderabad, India. The pressed pellets prepared by pressing collapsible aluminium cups of diameter 4 cm, containing 2 g of powdered samples along with boric acid under a hydraulic press (Hydraulic Press, Herzog, Germany) at 25 ton pressure; were further analysed for major oxide concentration using X-ray fluorescence spectroscopy (PANalytical Axios mAX4). The method for preparation of pellets and the protocol followed during analysis was adopted from ref. 65. Certified standard materials, MAG-1 (from United State Geological Survey), MESS-3 and PACS-2 (from National Research Council of Canada) were used to check the accuracy of the obtained results. The precision of the analyses is better than 3% for all major element oxides.

The total inorganic carbon (TIC) content was determined using coulometry, a method that detects cell current to measure the carbon dioxide released during sample acidification. The dried samples were grounded using a mortar and pestle to ensure uniform particle size ($N = 29$). Before commencing the coulometric measurements, solutions of KOH and KI were prepared. For the KOH solution, 11.25 g of KOH was added to 25 ml of distilled water. A 15 ml portion of this solution was transferred to the pre-scrubber assembly of the acidification module after cleaning. The KI solution was prepared by dissolving 12.5 g of KI in 25 ml of distilled water, and 1–2 drops of glacial acetic acid were added to maintain pH levels. The prepared KOH and KI solutions were utilized in the pre- and post-scrubber assemblies to remove unwanted gases such as atmospheric CO_2 , H_2S , and halogens. A carrier gas was employed to transport the CO_2 produced from the reaction of carbon in the sample and hydrochloric acid into the coulometric cell. Within the coulometric cell, the CO_2 gas reacts with ethyl amine, forming 2-hydroxyethylcarbonic acid. The formation of this acid triggers a cell current that is directly proportional to the amount of acid generated. This measurement provides the total inorganic content present in the sample. UIC CM 5014 Coulometer was used to estimate the TIC in the bulk sediments at CSIR-NIO, Goa, India. Certified calcium carbonate powder was used to ensure the accuracy (accuracy: 1.14497%). The CaCO_3 weight percent was calculated by multiplying the inorganic carbon readings with the molecular weight CaCO_3/C ratio (i.e., 8.33). The formula to calculate calcium carbonate content is $\text{CaCO}_3\% = \text{TIC} \times (\text{Molecular weight of } \text{CaCO}_3 / \text{Atomic weight of Carbon})$.

The total carbon (TC) content was determined using the Thermo Scientific FLASH 2000 at CSIR-NIO in Goa, India. Prior to starting the instrument, air blanks and bypass samples were run to ensure accurate peak detection and timing. To verify accuracy, certified standard material 25-(Bis(5-tert-butyl-2-benzo-oxazol-2-yl) thiophene (BBOT) with known composition (72.53 %C, 6.09 %H, 6.51 %N, 7.43 %O, 7.44 %S) was used, and the accuracy of the obtained results were checked (C: 0.00276%). A regression line was developed using the BBOT standard, and correlation factors were determined for carbon. The samples were weighed into tin capsules, and all accessories used for preparing the tin capsules were cleaned with acetone after each sample. The sediment sample and standard were repeated for both coulometric and TC analyses after every ten sample measurements. The standard deviation was calculated using the repeated sample, assuming a consistent measurement error for that particular cycle. Total organic carbon content was calculated by subtracting TIC from total TC.

Magnetic mineral extraction and electron microscopy

To extract detrital magnetic minerals from the bulk sediment samples, representative samples were selected. We followed ref. 3 method to extract the magnetic particles from the bulk sediment samples. Initially, the unconsolidated sediments were gently disintegrated in water and dispersed using ultrasonics. Sodium hexametaphosphate was added in small amounts to prevent the flocculation of clay minerals. The resulting sediment suspension was circulated within the magnetic mineral extraction setup. This circulation process was repeated multiple times to ensure the maximum removal of magnetic particles from the bulk sediment. The magnetic separates were washed several times using distilled water to remove the

adhered clay particles and placed in an ultrasonic bath (~10 min) prior to the imaging. The magnetic concentrates were then mounted on copper stubs. High-resolution scanning electron microscope (SEM) images and energy dispersive spectra (EDS) were obtained from these extracts at CSIR-NIO, Goa, India, using a JEOL JSM 5800 LV equipment equipped with a dispersive energy probe.

We followed ref. 35 method to extract the magnetic minerals from the bulk sediments specifically for the magnetofossils. Here, we provide a step-by-step account of our extraction process. Approximately 1.5 grams of sediment sample were first crushed using a clean mortar and pestle. One gram of the crushed sediment was then thoroughly mixed with 100 mL of distilled water in a 125 mL Erlenmeyer flask. To this mixture, 0.5 grams of anhydrous sodium carbonate (in granular form) were added. The Erlenmeyer flasks were securely placed on an orbital shaker set at 220 rpm for a duration of ~4 h. Subsequently, a rare earth magnet was positioned just above the curvature of each flask, and the flasks were once again placed on the orbital shaker at 220 rpm, this time for an extended period of ~20 h. Any excess clay material in suspension, found opposite to the magnet, was carefully removed using a pipette and transferred into a separate beaker. Following this, 50 mL of distilled water was added to the original flask. The flask was subjected to agitation on the shaker at 220 rpm for an additional hour. The material was then allowed to settle. After settling, the excess water was extracted from the flask and replaced with fresh distilled water. This procedure was repeated at least three times to ensure the thorough and clean extraction of magnetic minerals. The magnetic material collected nearest to the magnet was carefully pipetted into two separate 1.5 mL vials for each sample. Subsequently, 10 microliters of the magnetic material were pipetted into a clean vial, to which 20 microliters of ethanol were added and mixed thoroughly. Finally, 1–3 drops of the resulting mixture were pipetted onto a transmission electron microscopy (TEM) copper grid with lacey carbon. A magnet was placed beneath the grid to facilitate the centring of magnetic particles, and the grids were left to dry.

TEM analysis was performed using a JEOL F200 200 kV TEM at the Materials Characterization and Processing Facility at Johns Hopkins University. It is equipped with dual JEOL light-element detectors designed for quantitative X-ray analysis. We performed HRTEM analyses to capture the lattice fringes, and also SAED for mineralogy/crystallography. Dimensional measurements were performed using ImageJ and Digital Micrograph. The lattice fringes were estimated on ImageJ using fast Fourier transform. The TEM grids were later used for scanning electron microscopy (SEM) analyses. These grids were affixed to a carbon dot on an SEM stub and coated with a 17 nm carbon film. SEM analyses were conducted using the FEI Nova NanoSEM 600 in ultra-high resolution mode at the National Museum of Natural History, Smithsonian Institution, Washington DC. SEM imaging was conducted in a secondary electron mode using 15 kV voltage. The ThermoFisher energy dispersive X-ray detector (EDS) was utilized to capture X-ray spectra on the surface of magnetic minerals.

Data availability

The data used in this study is available on CSIR-NIO repository. All data sets produced in this article are stored in CSIR-NIO Data Repository (<https://publication-data.nio.org/s/JJYf8YEgi7XGXyC>).

Received: 25 July 2023; Accepted: 6 February 2024;

Published online: 28 February 2024

References

1. Blakemore, R. P. Magnetotactic bacteria. *Annu. Rev. Microbiol.* **36**, 217–238 (1982).
2. Kirschvink, J. L. & Chang, S.-B. R. Ultrafine-grained magnetite in deep-sea sediments: possible bacterial magnetofossils. *Geology* **12**, 559 (1984).
3. Petersen, N., von Dobeneck, T. & Vali, H. Fossil bacterial magnetite in deep-sea sediments from the South Atlantic ocean. *Nature* **320**, 611–615 (1986).

4. Mann, S., Sparks, N. H. C., Frankel, R. B., Bazylinski, D. A. & Jannasch, H. W. Biomineralization of ferrimagnetic greigite (Fe₃S₄) and iron pyrite (FeS₂) in a magnetotactic bacterium. *Nature* **343**, 258–261 (1990).
5. Vasiliev, I. et al. Putative greigite magnetofossils from the Pliocene epoch. *Nat. Geosci.* **1**, 782–786 (2008).
6. Faivre, D. & Schüller, D. Magnetotactic bacteria and magnetosomes. *Chem. Rev.* **108**, 4875–4898 (2008).
7. Kopp, R. E. & Kirschvink, J. L. The identification and biogeochemical interpretation of fossil magnetotactic bacteria. *Earth Sci. Rev.* **86**, 42–61 (2008).
8. Hesse, P. P. Evidence for bacterial palaeoecological origin of mineral magnetic cycles in oxic and sub-oxic Tasman Sea sediments. *Mar. Geol.* **117**, 1–17 (1994).
9. He, K. & Pan, Y. Magnetofossil abundance and diversity as paleoenvironmental proxies: a case study from southwest Iberian margin sediments. *Geophys. Res. Lett.* <https://doi.org/10.1029/2020GL087165> (2020).
10. Chang, L. et al. Coupled microbial bloom and oxygenation decline recorded by magnetofossils during the Palaeocene–Eocene thermal maximum. *Nat. Commun.* **9**, 4007 (2018).
11. Larrasoána, J. C. et al. Magnetotactic bacterial response to Antarctic dust supply during the Palaeocene–Eocene thermal maximum. *Earth Planet Sci. Lett.* **333–334**, 122–133 (2012).
12. Zhang, Q. et al. Magnetotactic bacterial activity in the North Pacific ocean and its relationship to Asian dust inputs and primary productivity since 8.0 Ma. *Geophys. Res. Lett.* <https://doi.org/10.1029/2021GL094687> (2021).
13. Goswami, P. et al. Magnetotactic bacteria and magnetofossils: ecology, evolution and environmental implications. *npj Biofilms and Microbiomes.* **8**, 43 (2022).
14. Blakemore, R. P. et al. South-seeking magnetotactic bacteria in the southern hemisphere. *Nature* **286**, 384–385 (1980).
15. Pan, Y. et al. Reduced efficiency of magnetotaxis in magnetotactic coccoid bacteria in higher than geomagnetic fields. *Biophys. J.* **97**, 986–991 (2009).
16. Chang, L. et al. Giant magnetofossils and hyperthermal events. *Earth Planet Sci. Lett.* **351–352**, 258–269 (2012).
17. Roberts, A. P. et al. Magnetotactic bacterial abundance in pelagic marine environments is limited by organic carbon flux and availability of dissolved iron. *Earth Planet Sci. Lett.* **310**, 441–452 (2011).
18. Kent, D. V. et al. A case for a comet impact trigger for the Paleocene–Eocene thermal maximum and carbon isotope excursion. *Earth Planet Sci. Lett.* **211**, 13–26 (2003).
19. Cramer, B. S. & Kent, D. V. Bolide summer: the Paleocene–Eocene thermal maximum as a response to an extraterrestrial trigger. *Palaeogeogr. Palaeoclimatol. Palaeoecol.* **224**, 144–166 (2005).
20. Kopp, R. E. et al. An Appalachian Amazon magnetofossil evidence for the development of a tropical river-like system in the mid-Atlantic United States during the Paleocene–Eocene thermal maximum. *Paleoceanogr. Palaeoclimatol. Palaeoecol.* <https://doi.org/10.1029/2009PA001783> (2009).
21. Zhang, Q., Liu, Q., Li, J. & Sun, Y. An integrated study of the eolian dust in pelagic sediments from the North Pacific ocean based on environmental magnetism transmission electron 447 microscopy and diffuse reflectance spectroscopy. *J. Geophys. Res. Solid Earth.* **123**, 3358–3376 (2018).
22. Lippert, P. C. & Zachos, J. C. A biogenic origin for anomalous fine-grained magnetic material at the Paleocene–Eocene boundary at Wilson Lake, New Jersey. *Paleoceanography* <https://doi.org/10.1029/2007PA001471> (2007).
23. Kopp, R. E. et al. Magnetofossil spike during the Paleocene–Eocene thermal maximum: ferromagnetic resonance, rock magnetic, and electron microscopy evidence from Ancora, New Jersey, United States. *Paleoceanography*. <https://doi.org/10.1029/2007PA001473> (2007).
24. Tarduno, J. A. Temporal trends of magnetic dissolution in the pelagic realm: gauging paleoproductivity. *Earth Planet Sci. Lett.* **123**, 39–48 (1994).
25. Lean, C. M. B. & McCave, I. N. Glacial to interglacial mineral magnetic and palaeoceanographic changes at Chatham Rise, SW Pacific Ocean. *Earth Planet Sci. Lett.* **163**, 247–260 (1998).
26. Yamazaki, T. & Kawahata, H. Organic carbon flux controls the morphology of magnetofossils in marine sediments. *Geology* **26**, 1064 (1998).
27. Yamazaki, T. Environmental magnetism of Pleistocene sediments in the North Pacific and Ontong-Java Plateau: temporal variations of detrital and biogenic components. *Geochem. Geophys. Geosys.* <https://doi.org/10.1029/2009GC002413> (2009).
28. Yamazaki, T. Paleoposition of the intertropical convergence zone in the eastern Pacific inferred from glacial–interglacial changes in terrigenous and biogenic magnetic mineral fractions. *Geology* **40**, 151–154 (2012).
29. Savian, J. F. et al. Enhanced primary productivity and magnetotactic bacterial production in response to middle Eocene warming in the Neo-Tethys Ocean. *Palaeogeogr. Palaeoclimatol. Palaeoecol.* **414**, 32–45 (2014).
30. Yamazaki, T. & Shimono, T. Abundant bacterial magnetite occurrence in oxic red clay. *Geology* **41**, 1191–1194 (2013).
31. Zhou, X. et al. Expanded oxygen minimum zones during the late Paleocene–early Eocene: hints from multiproxy comparison and ocean modeling. *Paleoceanogr. Palaeoclimatol. Palaeoecol.* **31**, 1532–1546 (2016).
32. Winguth, A. M. E., Thomas, E. & Winguth, C. Global decline in ocean ventilation, oxygenation, and productivity during the Paleocene–Eocene thermal maximum: implications for the benthic extinction. *Geology* **40**, 263–266 (2012).
33. Schumann, D. et al. Gigantism in unique biogenic magnetite at the Paleocene–Eocene thermal maximum. *Proc. Natl. Acad. Sci. USA* **105**, 17648–17653 (2008).
34. Wagner, C. L. et al. In situ magnetic identification of giant, needle-shaped magnetofossils in Paleocene–Eocene thermal maximum sediments. *Proc. Natl. Acad. Sci. USA* **118**, e2018169118 (2021).
35. Wagner, C. L. et al. Diversification of iron-biomineralizing organisms during the Paleocene–Eocene thermal maximum: evidence from quantitative unmixing of magnetic signatures of conventional and giant magnetofossils. *Paleoceanogr. Palaeoclimatol. Palaeoecol.* **36**, e2021PA004225 (2021).
36. Wang, H., Wang, J., Chen-Wiegart, Y. K. & Kent, D. V. Quantified abundance of magnetofossils at the Paleocene–Eocene boundary from synchrotron-based transmission X-ray microscopy. *Proc. Natl. Acad. Sci. USA* **112**, 12598–12603 (2015).
37. Xue, P., Chang, L., Pei, Z. & Harrison, R. J. Discovery of giant magnetofossils within and outside of the Paleocene–Eocene thermal maximum in the North Atlantic. *Earth Planet Sci. Lett.* **584**, 117417 (2022).
38. Egli, R. Characterization of individual rock magnetic components by analysis of remanence curves, 1. unmixing natural sediments. *Stud. Geophys. Geod.* **48**, 391–446 (2004).
39. Kobayashi, A. et al. Experimental observation of magnetosome chain collapse in magnetotactic bacteria: sedimentological, paleomagnetic, and evolutionary implications. *Earth Planet Sci. Lett.* **245**, 538–550 (2006).
40. Amor, M. et al. Key signatures of magnetofossils elucidated by mutant magnetotactic bacteria and micromagnetic calculations. *J. Geophys. Res. Solid Earth.* **127**, e2021JB023239 (2022).
41. Berndt, T. A., Chang, L. & Pei, Z. Mind the gap: Towards a biogenic magnetite palaeoenvironmental proxy through an extensive finite-element micromagnetic simulation. *Earth Planet Sci. Lett.* **532**, 116010 (2020).
42. Muxworthy, A. R., & Williams, W. Critical single-domain/multidomain grain sizes in noninteracting and interacting elongated magnetite

- particles: implications for magnetosomes. *J. Geophys. Res. Solid Earth*. <https://doi.org/10.1029/2006JB004588> (2006).
43. Nilsson-Kerr, K. et al. Indian summer monsoon variability 140–70 thousand years ago based on multi-proxy records from the Bay of Bengal. *Quaternary Sci. Rev.* **279**, 107403 (2022).
 44. Ota, Y. et al. Millennial-scale variability of Indian summer monsoon constrained by the western Bay of Bengal sediments: implication from geochemical proxies of sea surface salinity and river runoff. *Glob. Planet. Change*. **208**, 103719 (2022).
 45. Jousain, R. et al. Climatic control of sediment transport from the Himalayas to the proximal NE Bengal fan during the last glacial-interglacial cycle. *Quaternary Sci. Rev.* **148**, 1–16 (2016).
 46. Panmei, C., Naidu, P. D. & Naik, S. S. Variability of terrigenous input to the Bay of Bengal for the last ~ 80 kyr: implications on the Indian monsoon variability. *Geo-Marine Lett.* **38**, 341–350 (2018).
 47. Pattan, J. N. et al. Coupling between suboxic condition in sediments of the western Bay of Bengal and southwest monsoon intensification: a geochemical study. *Chem. Geol.* **343**, 55–66 (2013).
 48. Li, J. et al. Sedimentary responses to the sea level and Indian summer monsoon changes in the central Bay of Bengal since 40 ka. *Mar. Geol.* **415**, 105947 (2019).
 49. Gilly, W. F., Beman, J. M., Litvin, S. Y. & Robison, B. H. Oceanographic and biological effects of shoaling of the oxygen minimum zone. *Annu. Rev. Mar. Sci.* **5**, 393–420 (2013).
 50. Naqvi, S. W. Oxygen deficiency in the north Indian Ocean. *Gayana* **70**, 53–58 (2006).
 51. Rixen, T. et al. Reviews and syntheses: present, past and future of the oxygen minimum zone in the northern Indian Ocean. *Biogeosciences* **17**, 6051–6080 (2020).
 52. Johnson, K. S., Riser, S. C. & Ravichandran, M. Oxygen variability controls denitrification in the Bay of Bengal oxygen minimum zone. *Geophys. Res. Lett.* **46**, 804–811 (2019).
 53. Bristow, L. A. et al. N₂ production rates limited by nitrite availability in the Bay of Bengal oxygen minimum zone. *Nat. Geosci.* **10**, 24–29 (2017).
 54. Sarma, V. V. S. S. & Udaya Bhaskar, T. V. S. Ventilation of oxygen to oxygen minimum zone due to anticyclonic eddies in the Bay of Bengal. *J. Geophys. Res. Biogeosci.* **123**, 2145–2153 (2018).
 55. Verma, K. et al. Monsoon-related changes in surface hydrography and productivity in the Bay of Bengal over the last 45 kyr BP. *Palaeogeogr. Palaeoclimatol. Palaeoecol.* **589**, 110844 (2022).
 56. Govil, P. & Naidu, P. D. Variations of Indian monsoon precipitation during the last 32 kyr reflected in the surface hydrography of the Western Bay of Bengal. *Quat. Sci. Rev.* **30**, 3871–3879 (2011).
 57. Prajith, A., Tyagi, A. & Kurian, P. J. Influences of summer monsoon variations on the terrigenous influx, bioproductivity and early diagenetic changes in the southwest Bay of Bengal during late quaternary. *Mar. Geol.* **449**, 106825 (2022).
 58. Sebastian, T., Nath, B. N., Miriyala, P., Linsy, P. & Kocherla, M. Climatic control on detrital sedimentation in the continental margin off Chennai, western Bay of Bengal—A 42 kyr record. *Palaeogeogr. Palaeoclimatol. Palaeoecol.* **609**, 111313 (2023).
 59. Sarathchandraprasad, T. & Banarkar, V. K. Last 42 Ky Sediment chemistry of oxygen deficient coastal region of the Bay of Bengal: implications for terrigenous input and monsoon variability. *Curr. Sci.* **114**, 1940 (2018).
 60. Dutta, K., Bhushan, R. & Somayajulu, B. L. K. ΔR Correction values for the Northern Indian ocean. *Radiocarbon* **43**, 483–488 (2001).
 61. Egli, R. VARIFORC: An optimized protocol for calculating non-regular first-order reversal curve (FORC) diagrams. *Glob. Planet. Change*. **110**, 302–320 (2013).
 62. Harrison, R. J., & Feinberg, J. M. FORCinel: An improved algorithm for calculating first-order reversal curve distributions using locally weighted regression smoothing. *Geochem. Geophys. Geosys.* <https://doi.org/10.1029/2008GC001987> (2008).
 63. Weltje, G. J. End-member modeling of compositional data: numerical-statistical algorithms for solving the explicit mixing problem. *Math. Geol.* **29**, 503–549 (1997).
 64. Heslop, D. & Dillon, M. Unmixing magnetic remanence curves without a priori knowledge. *Geophys. J. Int.* **170**, 556–566 (2007).
 65. Krishna, K., Murthy, N. & Govil, P. Multielement analysis of soils by wavelength-dispersive X-ray fluorescence spectrometry. *At. Spectrosc.* **28**, 202–214 (2007).
 66. Tozer, B. et al. Global bathymetry and topography at 15 Arc Sec: SRTM15+. *Earth Space Sci.* **6**, 1847–1864 (2019).

Acknowledgements

The authors are grateful to the Director, CSIR-National Institute of Oceanography, Goa, India for providing the permission to publish this research work. We acknowledge the support of the project members and the ship cell personnel of CSIR-NIO for providing assistance in the collection of sediment core (SSK-50/GC-14A) as a part of project GEOSINKS- CSIR XII Plan projects GEOSINKS (PSC0106) during the scientific expedition SSK-50 onboard research vessel R/V Sindhu Sankalp of CSIR-NIO. We thank Dr. Nagender Nath B for providing access to the sediment core (SSK-50/GC-14A). Authors sincerely thank the Director, CSIR-National Geophysical Research Institute, Hyderabad, India for providing access to the Paleomagnetic and XRF facility. The authors sincerely acknowledge the facilities received from Central Analytical Facility (CAF), CSIR-NIO. We thank Areef Sardar for providing assistance with SEM-EDS analyses at CSIR-NIO. This is a part of Ph.D. thesis of Nitin Kadam. He is thankful to the Council of Scientific and Industrial Research, India for providing Senior Research Fellowship (31/026(0346)/2020-EMR-I) and the Smithsonian Institution for providing a Peter Buck Predoctoral Fellowship to Nitin Kadam. We thank Kenneth Livi for his help in acquiring the TEM data. We thank Tim Gooding for his assistance during SEM analyses. Authors are thankful to CSIR, India for funding the project “Long-term evolution of monsoon and associated processes” (LEMAP, MLP-2014). We wish to convey our thanks to the editor, Joe Aslin, the reviewer, Joseph Kirschvink, and the other anonymous reviewers for their insightful comments. This is CSIR-NIO publication no 7195.

Author contributions

N.K. conceived the research, performed sample analysis, data curation, data analysis, figure preparation, manuscript writing and editing; F.B., I.L. and C.L.W. conducted data analysis, manuscript writing and editing; F.B. and I.L. supervised the research; V.G., A.S., S.S. and M.V. performed data curation, data analysis.

Competing interests

The authors declare no competing interests.

Additional information

Supplementary information The online version contains supplementary material available at <https://doi.org/10.1038/s43247-024-01259-0>.

Correspondence and requests for materials should be addressed to Nitin Kadam or Firoz Badesab.

Peer review information *Communications Earth & Environment* thanks Joseph Kirschvink and the other, anonymous, reviewer(s) for their contribution to the peer review of this work. Primary Handling Editor: Joe Aslin. A peer review file is available.

Reprints and permissions information is available at <http://www.nature.com/reprints>

Publisher's note Springer Nature remains neutral with regard to jurisdictional claims in published maps and institutional affiliations.

Open Access This article is licensed under a Creative Commons Attribution 4.0 International License, which permits use, sharing, adaptation, distribution and reproduction in any medium or format, as long as you give appropriate credit to the original author(s) and the source, provide a link to the Creative Commons licence, and indicate if changes were made. The images or other third party material in this article are included in the article's Creative Commons licence, unless indicated otherwise in a credit line to the material. If material is not included in the article's Creative Commons licence and your intended use is not permitted by statutory regulation or exceeds the permitted use, you will need to obtain permission directly from the copyright holder. To view a copy of this licence, visit <http://creativecommons.org/licenses/by/4.0/>.

© The Author(s) 2024